INTERNATIONAL JOURNAL FOR NUMERICAL METHODS IN ENGINEERING
Int. J. Numer. Meth. Engng 2013; **93**:420–442
DOI: 10.1002/nme.4391

An augmented Lagrangian technique combined with a mortar algorithm for modelling mechanical contact problems

F. J. Cavalieri and A. Cardona*,†

Centro Internacional de Métodos Computacionales en Ingeniería (CIMEC-INTEC) CONICET-UNL,
Güemes 3450, S3000GLN Santa Fe, Argentina

SUMMARY

A finite element formulation for three dimensional (3D) contact mechanics using a mortar algorithm combined with a mixed penalty–duality formulation from an augmented Lagrangian approach is presented. In this method, no penalty parameter is introduced for the regularisation of the contact problem. The contact approach, based on the mortar method, gives a smooth representation of the contact forces across the bodies interface, and can be used in arbitrarily curved 3D configurations. The projection surface used for integrating the equations is built using a local Cartesian basis defined in each contact element. A unit normal to the contact surface is defined locally at each element, simplifying the implementation and linearisation of the equations. The displayed examples show that the algorithm verifies the contact patch tests exactly, and is applicable to large displacements problems with large sliding motions. Copyright © 2012 John Wiley & Sons, Ltd.

Received 18 November 2011; Revised 13 June 2012; Accepted 14 June 2012

KEY WORDS: contact mechanics; augmented Lagrangian; mortar method; mixed penalty-duality approach; finite elements

1. INTRODUCTION

Contact mechanics is used in many mechanical engineering branches, and numerous works have been dedicated to the numerical solution of contact problems applications: for instance, the design of gears [1], metal forming processes [2], contact fatigue [3] and others. New advances and techniques, including friction, large displacements, plasticity, and wear, are constantly being introduced. However, there is not yet a completely robust contact algorithm suitable for a wide range of applications in contact mechanics.

The relative displacement of two contacting bodies is currently described in the framework of the FEM using the so-called node–segment and segment–segment approaches. State-of-the-art reviews on computational contact mechanics can be found in [4, 5].

The classical node–segment technique is widely used in many commercial finite element codes. In this case, a node of one body (the slave), is associated with a segment or a surface of another body (the master) [6]. The main drawback of the node–segment approach is that it is not able to transmit a constant stress field from one body to the other when the meshes are nonconforming, that is, it does not pass the contact patch tests, and therefore introduces errors in the solutions independently of the mesh discretisation of the contacting bodies [7]. Furthermore, when the slave nodes slide from one to another master segment, the solution shows jumps in the contact stress field due to the enforcement of the discrete contact constraints.

---

*Correspondence to: A. Cardona, Centro Internacional de Métodos Computacionales en Ingeniería (CIMEC-INTEC) CONICET-UNL, Güemes 3450, S3000GLN Santa Fe, Argentina.

†E-mail: acardona@intec.unl.edu.ar

The two-pass node–segment method [8] satisfies the contact patch tests, but it can ‘lock’ due to the over constraints introduced in the formulation. Furthermore, it does not fulfil the Babuska–Brezzi conditions, and therefore produces ill-conditioned matrices and poor convergence rate, as shown by Puso and Laursen [9]. This approach is often selected for solving two-dimensional (2D) problems and certain three-dimensional (3D) mesh configurations, but it is not able to satisfy the contact patch test with quadratic or higher order elements [10, 11].

The difficulties associated with the node–segment approaches are overcome by using the segment–segment approaches and their variants. The first publication showing this technique was applied to 2D examples, and was then extended to 3D cases [12–14]. The mortar algorithm was initially proposed as a domain decomposition method, and was used to solve finite element problems with nonconforming discretisations [12, 15]. Bernardi *et al.* [16] published one of the first works using the mortar method and proved the satisfaction of the Babuska–Brezzi condition. Puso and Laursen proposed a contact algorithm based on the mortar method for 3D and large displacements problems [9, 17, 18]. In another work, Puso presented a mortar version with C^1 continuity of the contact interface, which was applicable to regular meshes only [19]. In most cases, the segment–segment algorithms use a projection surface for 3D problems, or a projection segment for 2D, in which all computations are performed.

One of the first techniques applied for regularising the contact problem was the penalty method [4], in which the displacement is the only primary variable in the formulation, leading to relatively easy numerical implementation. However, the exact solution is obtained only for an infinite value of the penalty constant. In a computational frame, high penalty values lead to ill-conditioned matrices and severe precision losses in the computations. In practice, several tests have to be carried out to find an appropriate value of the penalty for each problem.

Nonlinear contact mechanics can be related to nonlinear optimisation problems using inequality constraints, which allow the use of formulations with a more solid mathematical basis than the penalty method. The regularisation can be formulated using the method of Lagrange multipliers, which results in a saddle point system to be solved at each iteration. The Lagrange multipliers are used to enforce constraints, overcoming the ill-conditioning inconvenience of penalty methods at the expense of an increase in the size of the system of equations to solve. A combination of the penalty and the Lagrange multipliers techniques leads to the so-called augmented Lagrangian methods [20]. The augmented Lagrangian method was proposed first by Hestenes and Powell [21, 22] to solve optimisation problems with equality constraints, and then extended to inequality constraints, such as the contact problem by Rockafellar [23]. The addition of the penalty term to the Lagrangian constraints allows to obtain a convex objective function, which improves convergence far from the solution. Although both the augmented Lagrangian and the penalty methods require a penalty parameter, the role of a penalty in the augmented Lagrangian method is only to improve the convergence rate without influencing the accuracy of the computed solution.

The penalty technique combined with mortar-based formulations has been proposed in the works of Puso and Laursen [9], Puso *et al.* [17] and Yang *et al.* [24]. In all of these formulations, the exact solution is obtained only for an infinite value of penalty, which leads to ill-conditioned matrices. To overcome this problem, Puso *et al.* [18] proposed a mortar algorithm within an augmented Lagrangian scheme based on the double loop Uzawa type algorithm.

Usually, contact is modelled with the Lagrangian method in combination with an Uzawa type algorithm [20]. In this double loop algorithm, the Lagrange multipliers are held constant during an inner iteration loop for solving the displacements. Then, within an outer loop, the Lagrange multipliers are updated to a new value and the inner iteration is started again until convergence of the full process. This strategy, combined with a mortar method, was employed by Puso and Laursen [18] using standard shape functions for interpolating the Lagrange multipliers field.

Wohlmuth *et al.* [25] and Popp *et al.* [26] proposed to use the so-called dual shape functions for the interpolation of the Lagrange multipliers. In this case, the nodal values of the Lagrange multipliers are eliminated from the system of equations because of the special orthogonality properties of the interpolation shape functions involved. One advantage of this method is that the resulting system of equations remains constant. The proper subset of active and inactive nodes has to be found via a special active set strategy [25].

DOI: 10.1002/nme

An augmented Lagrangian method to solve contact problems with friction was proposed by Alart and Curnier [27] based on a reformulation of the contact and friction laws into a system of equations without inequalities. Christensen *et al.* [28] presented a modified version to solve the contact problem in the frame of small deformations. An improved version to solve elasto-plastic frictional contact problem using the so-called semi-smooth Newton was presented by Christensen [29]. Friction and frictionless contact problems using dual Lagrange multipliers and active set strategies are used in references [30–32]. In the work of Hager and Wohlmuth [33], they presented a formulation for the numerical treatment of frictional contact in combination with elasto-plasticity using a semi-smooth Newton method. For linear hardening laws, this method is a generalisation of the well-known radial return mapping.

In this work, the augmented Lagrangian approach proposed by Alart and Curnier [27] is used to formulate the frictionless contact problem in combination with the mortar method, which is used to define contact kinematics. The adopted form of the augmented Lagrangian approach allows the regularisation of non-differentiable contact terms, giving a C^1 differentiable saddle-point functional. The resulting equations involving the Lagrange multipliers are linearised and solved using a standard *Newton–Raphson*-like method. Contact kinematics are defined by using the mortar method, allowing the compatibility condition to be enforced along the contact interface and to verify the contact patch test, leading to a correct representation of the stress fields across the contact interface [34]. A similar approach has been followed in a recent paper by De Lorenzis *et al.* [35], but using a non-uniform rational B-spline (NURBS)-based isogeometric analysis.

Numerical examples that show that the algorithm satisfies the contact patch tests and exactly fulfils the contact constraints are presented. Two contact problems in the regime of large displacements demonstrate the applicability and robustness of the proposed algorithm. Finally, the algorithm is used in an industrial application, the contact of an internal combustion engine valve with its seat, showing smoothness in the computed contact stress field.

2. PROBLEM DESCRIPTION

The motion of the two bodies in contact $\mathcal{B}^\alpha$, $\alpha = 1, 2$, with domains Ω^α, is represented by the mappings $\chi^\alpha : \Omega^\alpha \times [0, T] \longrightarrow \mathbb{R}^3$, where current particle positions are identified by $\mathbf{x}^\alpha = \chi^\alpha(\mathbf{X}^\alpha, t)$. The contact interface between bodies, Γ_c, is given by the intersection of the two portions Γ_c^1 and Γ_c^2 of the external boundaries of $\mathcal{B}^1$ and $\mathcal{B}^2$, respectively, that can possibly enter into contact: $\Gamma_c = \Gamma_c^1 \cap \Gamma_c^2$. The potential energy of the contact constraint for the two deformable bodies is given by

$$\Pi^c = \sum_{\alpha=1}^{2} \int_{\Gamma_c^\alpha} \boldsymbol{t}^\alpha \cdot \boldsymbol{x}^\alpha \, \mathrm{d}\Gamma, \tag{1}$$

where $\boldsymbol{t}^\alpha$ is the Cauchy traction vector of the body $\mathcal{B}^\alpha$. Assuming linear momentum balance across the contact interface Γ_c^α, that is $\boldsymbol{t}^1 \, \mathrm{d}\Gamma = -\boldsymbol{t}^2 \, \mathrm{d}\Gamma$, the contact potential energy is expressed as follows:

$$\Pi^c = \int_{\Gamma_c^1} \boldsymbol{t}^1 \cdot (\mathbf{x}^1 - \boldsymbol{x}^2) \, \mathrm{d}\Gamma. \tag{2}$$

The FEM is used for discretising the domains of the bodies. The contact surfaces at each body and the traction vector can be parameterised as follows [9]:

$$\boldsymbol{x}^\alpha = \sum_{A=1}^{n^\alpha} N_A^\alpha(\boldsymbol{\xi}^\alpha) \boldsymbol{x}_A^\alpha, \quad \alpha = 1, 2, \qquad \boldsymbol{t}^1 = \sum_{A=1}^{n^1} N_A^1(\boldsymbol{\xi}^1) \boldsymbol{t}_A^1, \tag{3}$$

where $\boldsymbol{x}_A^\alpha \in \Gamma_c^\alpha \to \mathbb{R}^3$ are the nodal coordinates, n^α is the number of nodes in Γ_c^α, and $N_A^\alpha : \Gamma_c^\alpha \to \mathbb{R}$ are the classical finite element shape functions. The Cauchy traction vector $\boldsymbol{t}^1$, Equation $(3)_2$, is discretised with the same standard shape functions used to approximate the geometry and the displacements on the surface Γ_c^1.

As they are customarily called in the literature, Γ_c^1 and Γ_c^2 are the *non-mortar* and *mortar* surfaces, respectively. Assuming frictionless contact, and using Equations (2) and (3), the contact potential energy can be approximated as

$$\Pi^c = \sum_{A=1}^{n^1} \boldsymbol{t}_A \cdot [\boldsymbol{\nu}_A \otimes \boldsymbol{\nu}_A] \left(\sum_{B=1}^{n^1} \int_{\Gamma_c^1} N_A^1(\boldsymbol{\xi}^1) N_B^1(\boldsymbol{\xi}^1) \,\mathrm{d}\Gamma \, \boldsymbol{x}_B^1 - \sum_{C=1}^{n^2} \int_{\Gamma_c^1} N_A^1(\boldsymbol{\xi}^1) N_C^2(\boldsymbol{\xi}^2) \,\mathrm{d}\Gamma \, \boldsymbol{x}_C^2 \right), \tag{4}$$

with $\boldsymbol{\nu}_A$ being the inward normal vector to the non-mortar contact interface Γ_c^1 at node A.

The *mortar interpenetration* $\boldsymbol{g}_A$ is defined by

$$\boldsymbol{g}_A = \sum_{B=1}^{n^1} n_{AB}^1 \, \boldsymbol{x}_B^1 - \sum_{C=1}^{n^2} n_{AC}^2 \, \boldsymbol{x}_C^2, \tag{5}$$

where

$$n_{AB}^1 = \int_{\Gamma_c^1} N_A^1(\boldsymbol{\xi}^1) N_B^1(\boldsymbol{\xi}^1) \,\mathrm{d}\Gamma, \qquad n_{AC}^2 = \int_{\Gamma_c^1} N_A^1(\boldsymbol{\xi}^1) N_C^2(\boldsymbol{\xi}^2) \,\mathrm{d}\Gamma, \tag{6}$$

are the *weight factors* of either side. Vector $\boldsymbol{g}_A$ can be interpreted as an integrated interpenetration measure, which corresponds to the zone linked to the non-mortar node A. The contribution to the normal interpenetration at node A is obtained by projection on the normal direction at the same node:

$$g_{NA} = \boldsymbol{\nu}_A \cdot \boldsymbol{g}_A, \tag{7}$$

whereas projection on the Cauchy traction vector on the normal direction gives the normal component of the Cauchy traction

$$t_{NA} = \boldsymbol{\nu}_A \cdot \boldsymbol{t}_A. \tag{8}$$

The contact potential energy, Equation (4), is then written in the following form:

$$\Pi^c = \sum_{A=1}^{n^1} t_{NA} g_{NA}. \tag{9}$$

The solution to the general frictionless unilateral contact problem, obtained by a mortar FEM formulation is finally given by

$$\begin{aligned} \boldsymbol{U} &= \operatorname{arginf}\,(\Pi^{\text{int}}(\boldsymbol{U}) + \Pi^{\text{ext}}(\boldsymbol{U}) + \Pi^c(\boldsymbol{U})), \\ &\text{s.t.} \quad g_{NA} \geqslant 0, \quad t_{NA} \geqslant 0, \quad t_{NA} g_{NA} = 0 \qquad A = 1, \dots n^1. \end{aligned} \tag{10}$$

where $\Pi^{\text{int,ext}}(\boldsymbol{U})$ are the potential energy terms due to internal and external forces, and $\boldsymbol{U}$ is the global displacements vector. The second line in Equation (10) states the Karush–Kuhn–Tucker (KKT) conditions for unilateral contact, which are expressed in discrete form at the non-mortar nodes A. The first condition is the geometric impenetrability constraint, the second inequality represents the non-traction condition at the contact interface (i.e. only the compression interaction is allowed), and the third one is the complementarity equation.

Instead of working with the normal component of traction, it is often preferred to work with the contact pressure field $p = -t_N$. In this case, the KKT conditions read as follows:

$$g_{NA} \geqslant 0, \qquad p_A \leqslant 0, \qquad p_A g_{NA} = 0 \qquad A = 1, \dots n^1. \tag{11}$$

The nodal pressures play the role of the Lagrange multipliers that enforce the impenetrability constraint. The contact problem (10), with either form of the KKT conditions, can be solved using a double loop Uzawa algorithm. Alternatively, a penalty method can be formulated by assuming the nodal pressures are linearly related to the normal penetration by a penalty constant. In the next section, an alternative solution scheme, which leads to a simple monolithic algorithm is proposed.

3. AUGMENTED LAGRANGIAN METHOD

The inequality constraints in Equations (11) can be equivalently written as the sub-differential inclusion

$$p_A \in \partial \Psi_{\boldsymbol{R}_+}(g_{NA}), \tag{12}$$

where $\Psi_{\boldsymbol{R}_+}$ is the indicator function of the real positive half line $\boldsymbol{R}_+$ and $\partial\Psi_{\boldsymbol{R}_+}$ is the sub-differential of $\Psi_{\boldsymbol{R}_+}$. Equation (12) expresses the unilateral contact conditions, with a contact pressure field derived from a non-smooth potential $\Psi_{\boldsymbol{R}_+}(g_{NA})$ [27, 36].

Equation (10) can be regularised and solved by using a mixed dual penalty approach based on an augmented Lagrangian method, as proposed by Alart and Curnier [27]. The potential energy of contact is replaced by an augmented Lagrangian function, which is defined by

$$\mathcal{L}^c(\boldsymbol{U},\boldsymbol{p}) = \mathcal{L}^c(\boldsymbol{\Phi}) = \sum_{A=1}^{n^1}\left(k p_A g_{NA} + \frac{r}{2} g_{NA}^2 - \frac{1}{2r} < k p_A + r g_{NA} >^2\right), \tag{13}$$

where r is a positive penalty parameter, k is a positive scale factor, and $< \cdot >$ is the Macauley bracket operator, that is,

$$< x > = \begin{cases} x & x \geqslant 0 \\ 0 & x < 0 \end{cases}$$

This functional is C^1 differentiable saddle-point, as shown in Figure 1. The solution is obtained as the set of values that render this functional stationary. The solution does not depend on the value of parameters r, k. Nevertheless, the convergence rate does depend on their value. In numerical computations, default values of r and k are selected in terms of a mean value of the Young modulus of the bodies in contact and of a mean value of mesh size, as follows:

$$r = k \approx 10\frac{E_{\text{mean}}}{h_{\text{mean}}} \tag{14}$$

Numerical examples show that this choice gives a better condition number of the iteration matrix than other choices. A numerical experiment is provided in the examples section, to illustrate on the influence of these parameters on the convergence properties.

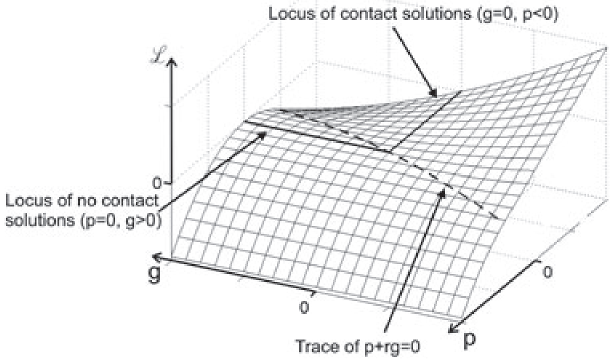

Figure 1. Augmented Lagrangian function for the contact problem. The locus of solutions is displayed.

After splitting the Macauley term according to the contact status of each zone, the Lagrangian can be written as follows

$$\mathcal{L}^c(\boldsymbol{\Phi}) = \sum_{A=1}^{n^1} \begin{cases} k\ p_A\, g_{NA} + \frac{r}{2} g_{NA}^2 & \text{if } k p_A + r g_{NA} \leqslant 0 \quad \text{(Contact zone)} \\ -\frac{k^2}{2r} p_A^2 & \text{if } k p_A + r g_{NA} > 0 \quad \text{(Gap zone)} \end{cases} \tag{15}$$

where p_A is the nodal value of the contact pressure, and plays the role of the Lagrange multiplier that enforces the contact condition. By differentiation of Equation (15), a nonlinear system of equations is obtained.

4. WEIGHT FACTORS COMPUTATION: DEFINITION OF THE CONTACT ELEMENT

The non-mortar surface Γ_c^1 and the mortar surface Γ_c^2 are parameterised in terms of the finite element shape functions of the solid elements of each body, which are next to the contact boundaries. The integrals necessary to calculate the weight factors n_{AB}^{α} are computed by assembling the contributions of all pairs of facet elements on either side.

In order to compute the weight factors, a local plane $\boldsymbol{p}$ is defined where the integrals on Γ_c^1 appearing in Equation (6) are performed. The numerical integration algorithm used is analogous to the one proposed by Puso and Laursen [9]. The non-mortar facet k and the mortar facet l, with nodal coordinates $\boldsymbol{x}_A^{\alpha}$, $\alpha = 1, 2$, respectively, are projected on the local plane $\boldsymbol{p}$, giving polygons $\tilde{k}$ and $\tilde{l}$ with coordinates $\boldsymbol{y}_A^{\alpha} \in \mathbb{R}^2$, $\alpha = 1, 2$.

The nodal coordinates of the non-mortar facet k are used to calculate the normal vector $\boldsymbol{e}_3$ that defines the plane $\boldsymbol{p}$ (see Figure 2(a)) and the Appendix for details). The unit vectors $\boldsymbol{e}_1, \boldsymbol{e}_2$ lying on the plane $\boldsymbol{p}$ are built by forming an orthonormal local basis $\{\boldsymbol{e}_1, \boldsymbol{e}_2, \boldsymbol{e}_3\}$. The nodal coordinates $\boldsymbol{y}_A^{\alpha} \in \mathbb{R}^2$ of the projected facets are given by

$$\boldsymbol{y}_A^{\alpha} = \begin{bmatrix} \boldsymbol{e}_1 \cdot \left(\boldsymbol{x}_A^{\alpha} - \boldsymbol{x}_1^1\right) \\ \boldsymbol{e}_2 \cdot \left(\boldsymbol{x}_A^{\alpha} - \boldsymbol{x}_1^1\right) \end{bmatrix}, \tag{16}$$

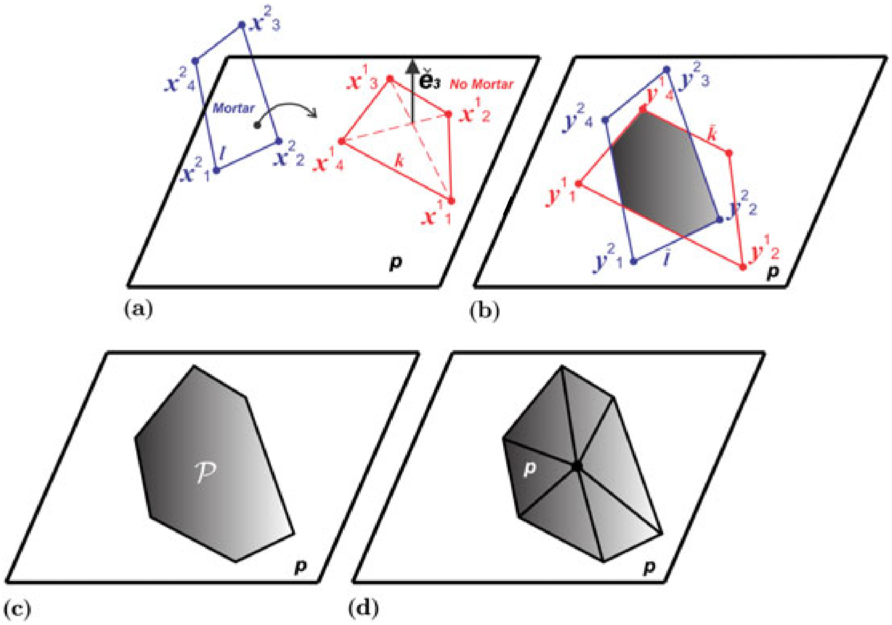

Figure 2. (a)Non-mortar facet k, mortar facet l, projection plane $\boldsymbol{p}$ with unit normal $\boldsymbol{e}_3$ and local basis $\mathcal{V} = \{\boldsymbol{e}_1, \boldsymbol{e}_2, \boldsymbol{e}_3\}$. (b) Facets k and l projected on the plane $\boldsymbol{p}$. (c) Intersection polygon $\mathcal{P}$. (d) Subdivision of polygon $\mathcal{P}$ into triangles.

where $\boldsymbol{x}_1^1$ is the coordinates vector of the first node of the non-mortar facet k (Figure 2(b)). When the facets k and l are in contact, the coordinates $\boldsymbol{y}_A^\alpha$ define an intersection polygon $\mathcal{P}$ whose shape depends on the way the facets are intersected (Figure 2(c)). The polygon $\mathcal{P}$ is calculated using an algorithm for the intersection of planar polygons based on advance rules with a parametric definition of segments [37]. The integrals in Equation (6) are then computed by subdividing the polygon $\mathcal{P}$ into triangles (Figure 2(d)). A Gauss integration rule is defined over each triangle, and the mortar and non-mortar shape functions are evaluated at the coordinates of the Gauss points of each triangle by projecting back the coordinates in the plane $\boldsymbol{p}$ of the evaluation point to each facet. Finally, the sum of the integrals on each triangle gives the weight factors n_{AB}^α.

In this work, the expression of nodal coordinates is defined in $\mathbb{R}^2$ by Equation (16). Linear momentum is conserved exactly as in Puso and Laursen [9].

A *contact element* is defined for each pair of facets, one on the non-mortar and the other on the mortar surface. If $N1$ is the number of facets on the surface Γ_c^1, and $N2$ is the number of facets on the surface Γ_c^2, a total of $N1 \times N2$ contact elements are built. Note however, that only a few of them are active at a given time (i.e. only those elements whose facets are seeing each other). At each contact element, the restrictions to the element facets of the integrals needed for the computation of the weight factors n_{AB}^1, n_{AB}^2 are evaluated. The problem weight factors are then obtained by assembling the contributions of all elements, as usual.

The generalised coordinates of the contact element are

$$\boldsymbol{\Phi}^e = \left[\boldsymbol{x}_1^{1^T}\ \boldsymbol{x}_2^{1^T}\ \dots\ \boldsymbol{x}_{m^1}^{1\ T}\ \boldsymbol{x}_1^{2^T}\ \boldsymbol{x}_2^{2^T}\ \dots\ \boldsymbol{x}_{m^2}^{2\ T}\ p_1\ p_2\ \dots\ p_{m^1}\right]^T, \tag{17}$$

where m^1 and m^2 are the number of nodes of the non-mortar facet and the mortar facet, respectively, $\boldsymbol{x}_I^1$ are the nodal coordinates of the non-mortar facet; $\boldsymbol{x}_I^2$ are the nodal coordinates of the mortar facet, and p_I are the contact nodal pressures. The number of DOFs of the contact element is $4m^1 + 3m^2$.

5. CONTACT ELEMENT INTERNAL FORCES VECTOR

The internal forces vector of the contact element is obtained taking variations of $\mathcal{L}^c$ with respect to the generalised coordinates $\delta\boldsymbol{\Phi}^e$ as follows:

$$\delta\mathcal{L}^c(\boldsymbol{\Phi}^e) = \sum_{A=1}^{m^1} \begin{cases} \eta_A \delta g_{NA} + k g_{NA} \delta p_A, & \text{if } \eta_A \leqslant 0 \\ -\frac{k^2}{r} p_A \delta p_A & \text{if } \eta_A > 0, \end{cases} \tag{18}$$

where $\eta_A = k p_A + r g_{NA}$ is the augmented Lagrange multiplier or augmented pressure, which fixes the state of contact or gap. The Equations (18) have both displacement and pressure (Lagrange multipliers) terms as unknowns. For this reason, the method is called a mixed or dual penalty method.

The variation of the normal gap is given by

$$\delta g_{NA} = \delta(\boldsymbol{g}_A \cdot \boldsymbol{\nu}_A) = \delta\boldsymbol{\nu}_A \cdot \boldsymbol{g}_A + \boldsymbol{\nu}_A \cdot \delta\boldsymbol{g}_A \tag{19}$$

Equation (19) is simplified due to the fact that at equilibrium $\boldsymbol{g}_A$ is parallel to $\boldsymbol{\nu}_A$, and therefore $\delta\boldsymbol{\nu}_A \cdot \boldsymbol{g}_A = 0$; for details, see for example, [4, 35]. Hence, the variation of the Lagrangian is written as follows:

$$\delta\mathcal{L}^c(\boldsymbol{\Phi}^e) = \sum_{A=1}^{m^1} \begin{cases} \eta_A \boldsymbol{\nu}_A \cdot \delta\boldsymbol{g}_A + k g_{NA} \delta p_A, & \text{if } \eta_A \leqslant 0 \\ -\frac{k^2}{r} p_A \delta p_A & \text{if } \eta_A > 0. \end{cases} \tag{20}$$

The internal forces vector of the contact element $\boldsymbol{F}^e_{\text{cont}}$ can then be readily identified as conjugated to the variation of generalised coordinates:

$$\delta\mathcal{L}^c(\boldsymbol{\Phi}^e) = \delta\boldsymbol{\Phi}^e \cdot \boldsymbol{F}^e_{\text{cont}}(\boldsymbol{\Phi}^e) = \sum_{A=1}^{m^1} \begin{bmatrix} \delta\boldsymbol{x}^1_B \\ \delta\boldsymbol{x}^2_C \\ \delta p_B \end{bmatrix} \cdot \begin{cases} \begin{bmatrix} \eta_A\, \boldsymbol{\nu}_A\, n^1_{AB} \\ -\eta_A\, \boldsymbol{\nu}_A\, n^2_{AC} \\ k g_{NA} \boldsymbol{\delta}_{AB} \end{bmatrix}, & \text{if } \eta_A \leqslant 0, \\ \begin{bmatrix} \boldsymbol{0} \\ \boldsymbol{0} \\ -\frac{k^2}{r} p_A \boldsymbol{\delta}_{AB} \end{bmatrix}, & \text{if } \eta_A > 0, \end{cases} \tag{21}$$

where $\boldsymbol{\delta}_{AB}$ is the Kronecker delta. The contact status at the zone related to node A is established in terms of the sign of $\eta_A = kp_A + rg_{NA}$. This expression is a linear combination of the primal and dual variables.

Equilibrium is obtained by solving the following nonlinear system of equations

$$\boldsymbol{G}(\boldsymbol{U}) + \boldsymbol{F}_{\text{cont}}(\boldsymbol{\Phi}) = \boldsymbol{0} \tag{22}$$

where $\boldsymbol{G}(\boldsymbol{U})$ is the nonlinear vector of internal and external structural forces and where $\boldsymbol{F}_{\text{cont}}(\boldsymbol{\Phi})$ is the set of contact forces at the interface Γ_c, which is obtained by assembling all contact element contributions $\boldsymbol{F}^e_{\text{cont}}$.

The system of equations (22) does not change during the iterations. In primal–dual active set strategies, the set of DOFs for which $\eta_A \leqslant 0$ is called *active set*, whereas those for which $\eta_A > 0$ form the *inactive set*. These strategies are equivalent to semi-smooth Newton methods [38]. The method of solution we implement is a semi-smooth Newton method with an augmented Lagrangian [27] combined with a mortar method for accurate representation of contact. Thanks to the C^1 continuity of $\mathcal{L}$, this system can be solved simultaneously for the displacements and for the Lagrange multipliers using a standard Newton–Raphson iterative monolithic scheme [35, 38, 39].

5.1. *Evaluation of the normal vector $\boldsymbol{\nu}_A$*

The normal vector at the vertex A is computed in terms of the cross product of edge vectors of the non-mortar facet. The edge vectors $\boldsymbol{v}_A$, $\boldsymbol{w}_A$ are defined, at any vertex A of the considered non-mortar facet, in the following form:

$$\begin{aligned} \boldsymbol{v}_A &= \boldsymbol{x}^1_J - \boldsymbol{x}^1_A, \\ \boldsymbol{w}_A &= \boldsymbol{x}^1_A - \boldsymbol{x}^1_K, \end{aligned} \tag{23}$$

where

$$J = \text{mod}(A, m^1) + 1, \qquad K = \text{mod}(A+1, m^1) + 1, \qquad A = 1, \dots m^1.$$

and where mod() is the modulo or remainder operation. Thus, the normal vector is calculated using

$$\boldsymbol{\nu}_A = \frac{\boldsymbol{v}_A \times \boldsymbol{w}_A}{\|\boldsymbol{v}_A \times \boldsymbol{w}_A\|}. \tag{24}$$

Note that two facets that share a common vertex A do not have the same definition for the normal vector at the vertex. In fact, the element internal force at node A can be seen as a contribution coming from a zone *inside* the element and close to the considered node. The total contribution to the node A is obtained by adding up all contributions from the neighbour elements, each one having its own direction. Some authors define a unique normal vector at the node, common to all elements that share the node. This increases severely the complexity of the computations, because neighbour elements become coupled.

DOI: 10.1002/nme

6. LINEARISATION OF INTERNAL FORCES OF CONTACT

The linearisation of Equation (21) leads to the tangent Hessian matrix of the contact element, which depends on the contact status:

$$\delta \boldsymbol{\Phi}^e \cdot \Delta \boldsymbol{F}^e_{\text{cont}} = \sum_{A=1}^{m^1} \begin{bmatrix} \Delta \boldsymbol{x}^1_B \\ \Delta \boldsymbol{x}^2_C \\ \Delta p_B \end{bmatrix} \cdot \begin{cases} \begin{bmatrix} (k\Delta p_A + r\Delta g_{NA})\boldsymbol{\nu}_A\, n^1_{AB} \\ \quad +\eta_A(\boldsymbol{\nu}_A\, \Delta n^1_{AB} + n^1_{AB}\Delta \boldsymbol{\nu}_A) \\ \\ -(k\Delta p_A + r\Delta g_{NA})\boldsymbol{\nu}_A\, n^2_{AC} \\ \quad -\eta_A(\boldsymbol{\nu}_A\, \Delta n^2_{AC} + n^2_{AC}\Delta \boldsymbol{\nu}_A) \\ \\ k\Delta g_{NA}\boldsymbol{\delta}_{AB} \end{bmatrix}, & \eta_A \leqslant 0 \\ \begin{bmatrix} \mathbf{0} \\ \mathbf{0} \\ -\dfrac{k^2}{r}\Delta p_A \boldsymbol{\delta}_{AB} \end{bmatrix}, & \eta_A > 0. \end{cases} \tag{25}$$

The explicit expression of the Hessian matrix is obtained by evaluating the first derivatives of the weight factors n^α_{AB}, the normal interpenetration g_{NA}, and the normal vector $\boldsymbol{\nu}_A$. These derivatives are presented in the following subsections.

6.1. Weight factors linearisation

The weight factors n^α_{AB} are computed by adding up the contributions $n^{\alpha,P}_{AB}$ from each triangle P of the polygon $\mathcal{P}$. Using Equation (6), the linearisation of the weight factors $n^{\alpha,P}_{AB}$ can be written as follows:

$$\begin{aligned} \Delta n^{\alpha,P}_{AB} &= \Delta \int_{\Gamma^1_c} N^1_A(\boldsymbol{\xi}^1) N^\alpha_B(\boldsymbol{\xi}^\alpha)\, \mathrm{d}\Gamma_c \\ &= \sum_{g=1}^{ng} \left[\Delta N^1_A\left(\boldsymbol{\xi}^1_g\right) N^\alpha_B\left(\boldsymbol{\xi}^\alpha_g\right) + N^1_A\left(\boldsymbol{\xi}^1_g\right) \Delta N^\alpha_B\left(\boldsymbol{\xi}^\alpha_g\right)\right] w_g A^P + n^{\alpha,P}_{AB} \frac{\Delta A^P}{A^P}, \end{aligned} \tag{26}$$

where ng is the number of Gauss points, $\boldsymbol{\xi}^\alpha_g$, $\alpha = 1, 2$, are the projection of the Gauss point coordinates on the non-mortar and mortar facet elements, respectively, and w_g are the integration weight factors. To compute Equation (26), the variations of the shape functions N^α_A and of the area A^P of each triangle P are calculated next.

6.1.1. Linearisation of the shape functions. The projection of the local coordinates $\boldsymbol{\xi}_g$ of a Gauss point in triangle P over the facet elements is established by the following equation:

$$\sum_{I=1}^{3} N^P_I(\boldsymbol{\xi}_g)\, \boldsymbol{y}^P_I = \sum_{A=1}^{m^\alpha} N^\alpha_A\left(\boldsymbol{\xi}^\alpha_g\right)\, \boldsymbol{y}^\alpha_A. \tag{27}$$

The subscript $I = 1 \ldots 3$ spans the three vertices of triangle P, whereas the subscript $A = 1 \ldots m^\alpha$ spans the vertices of the contact facets, which are $m^\alpha = 3$ for triangular facets and $m^\alpha = 4$ for quadrangular facets. When the facet elements are quadrangular, the unknowns, that is, the Gauss point coordinates $\boldsymbol{\xi}^\alpha_g$, are obtained by solving Equation (27) with a Newton–Raphson algorithm. Instead, when the facet elements are triangles, the coordinates $\boldsymbol{\xi}^\alpha_g$ are computed explicitly.

The increment of the shape function N^α_A at node A is obtained by taking partial derivatives of the shape functions in the direction ξ^α_β:

$$\Delta N^\alpha_A = \sum_{\beta=1}^{2} \frac{\partial N^\alpha_A}{\partial \xi^\alpha_\beta}\left(\boldsymbol{\xi}^\alpha_g\right)\, \Delta \xi^\alpha_\beta. \tag{28}$$

From Equation (27), the increment of the coordinate $\boldsymbol{\xi}^\alpha$ in the direction β is given by

$$\Delta\xi^\alpha_\beta = \boldsymbol{\tau}^{\alpha\,T}_\beta \left(\sum_{I=1}^{3} N_I^P(\boldsymbol{\xi}_g)\Delta \boldsymbol{y}_I^P - \sum_{A=1}^{m^\alpha} N_A^\alpha\left(\boldsymbol{\xi}_g^\alpha\right)\Delta\boldsymbol{y}_A^\alpha\right), \quad \beta = 1,2 \tag{29}$$

where

$$\boldsymbol{\tau}^{\alpha\,T}_\beta = \left[\sum_{A=1}^{m^\alpha} \frac{\partial N_A^\alpha}{\partial \xi_\beta^\alpha}\left(\boldsymbol{\xi}_g^\alpha\right)\ \boldsymbol{y}_A^\alpha\right]^{-1}. \tag{30}$$

In Equation (30), the coefficients $\boldsymbol{\tau}^\alpha_\beta$ are obtained by inverting a 2 × 2 matrix. By replacing Equation (29) into Equation (28), the variation of the shape function evaluated at the Gauss points $\boldsymbol{\xi}^\alpha_g$ can be written as follows:

$$\Delta N_A^\alpha\left(\boldsymbol{\xi}_g^\alpha\right) = \sum_{\beta=1}^{2} \frac{\partial N_A^\alpha}{\partial \xi_\beta^\alpha}\left(\boldsymbol{\xi}_g^\alpha\right)\ \boldsymbol{\tau}^{\alpha\,T}_\beta \left(\sum_{I=1}^{3} N_I^P(\boldsymbol{\xi}_g)\Delta \boldsymbol{y}_I^P - \sum_{A=1}^{m^\alpha} N_A^\alpha\left(\boldsymbol{\xi}_g^\alpha\right)\Delta\boldsymbol{y}_A^\alpha\right). \tag{31}$$

Equation (31) gives the variation of the shape function $\Delta N_A^\alpha\left(\boldsymbol{\xi}_g^\alpha\right)$ in terms of the variation of the nodal coordinates of triangle P, which is part of polygon $\mathcal{P}$. These coordinates are computed from the nodal coordinates of the projected non-mortar and mortar elements on the plane $\boldsymbol{p}$, by the polygons intersection algorithm. The nodal coordinates vectors $\boldsymbol{y}_A^\alpha \in \mathbb{R}^2$ of the projected elements $\tilde{k}$ and $\tilde{l}$ are put together forming vector $\boldsymbol{Y}$ in the form

$$\boldsymbol{Y} = \left[\begin{array}{cccccccc} \boldsymbol{y}_1^{1\,T} & \boldsymbol{y}_2^{1\,T} & \ldots & \boldsymbol{y}_{m^1}^{1\ \ T} & \boldsymbol{y}_1^{2\,T} & \boldsymbol{y}_2^{2\,T} & \ldots & \boldsymbol{y}_{m^2}^{2\ \ T} \end{array}\right]^T. \tag{32}$$

Then, the relationship between the increment of nodal coordinates of triangle P and the increment of nodal coordinates of the projected facet elements is given by

$$\Delta\boldsymbol{y}_I^P = \mathbf{D}_I^P\,\Delta\boldsymbol{Y} = \sum_{K=1}^{m^1} \mathbf{D}_{IK}^{P_1}\Delta\boldsymbol{y}_K^1 + \sum_{L=1}^{m^2} \mathbf{D}_{IL}^{P_2}\Delta\boldsymbol{y}_L^2. \tag{33}$$

Details about the matrix $\boldsymbol{D}_I^P$ are outlined in the Appendix. In Equation (33), the contributions to the nodal coordinates increment are separated in contributions $\boldsymbol{D}_{IK}^{P_1}\Delta\boldsymbol{y}_K^1$ coming from the non-mortar projected facet and contributions to increment $\boldsymbol{D}_{IL}^{P_2}\Delta\boldsymbol{y}_L^2$ coming from the mortar projected facet.

Finally, by using Equations (33), (29) and (30), the increment of the shape functions, Equation (31), is written as follows:

$$\Delta N_A^\alpha\left(\boldsymbol{\xi}_g^\alpha\right) = \boldsymbol{P}_A^{\alpha,P}\left(\boldsymbol{\xi}_g^\alpha\right)\ \Delta\boldsymbol{Y}, \tag{34}$$

where

$$\begin{aligned}
\boldsymbol{P}_A^{1,P} = \sum_{\beta=1}^{2}\left(N_{A,\beta}^1\,\boldsymbol{\tau}_\beta^{1\,T}\right)\Big[& N_I^P\boldsymbol{D}_{I1}^{P_1} - N_1^1\boldsymbol{I} \quad N_I^P\boldsymbol{D}_{I2}^{P_1} - N_2^1\boldsymbol{I} \quad \ldots \\
& N_I^P\boldsymbol{D}_{Im^1}^{P_1} - N_{m^1}^1\boldsymbol{I} \quad N_I^P\boldsymbol{D}_{I1}^{P_2} \quad N_I^P\boldsymbol{D}_{I2}^{P_2} \quad \ldots \quad N_I^P\boldsymbol{D}_{Im^2}^{P_2}\Big], \\
\boldsymbol{P}_A^{2,P} = \sum_{\beta=1}^{2}\left(N_{A,\beta}^2\,\boldsymbol{\tau}_\beta^{2\,T}\right)\Big[& N_I^P\boldsymbol{D}_{I1}^{P_1} \quad N_I^P\boldsymbol{D}_{I2}^{P_1} \quad \ldots \\
& N_I^P\boldsymbol{D}_{Im^1}^{P_1} \quad N_I^P\boldsymbol{D}_{I1}^{P_2} - N_1^2\boldsymbol{I} \quad N_I^P\boldsymbol{D}_{I2}^{P_2} - N_2^2\boldsymbol{I} \quad \ldots \quad N_I^P\boldsymbol{D}_{Im^2}^{P_2} - N_{m^2}^2\boldsymbol{I}\Big].
\end{aligned} \tag{35}$$

6.1.2. Triangle area linearisation. The triangle area variation, ΔA^P is also required to complete the linearisation process of the Equation (26). The area of a triangle $P \in \mathcal{P}$ is determined using the cross product of two vectors defined from the nodal coordinates $\boldsymbol{y}_I^P \in \mathbb{R}^2$,

$$A^P = \frac{1}{2}\left(\boldsymbol{y}_2^P - \boldsymbol{y}_1^P\right) \times \left(\boldsymbol{y}_3^P - \boldsymbol{y}_1^P\right) = \frac{1}{2}\widetilde{\left(\boldsymbol{y}_2^P - \boldsymbol{y}_1^P\right)}\left(\boldsymbol{y}_3^P - \boldsymbol{y}_1^P\right). \tag{36}$$

where $\widetilde{\boldsymbol{u}} = \begin{bmatrix} -u_2 & u_1 \end{bmatrix} \mid \boldsymbol{u} \times \boldsymbol{v} = \widetilde{\boldsymbol{u}}\boldsymbol{v} = -\boldsymbol{v} \times \boldsymbol{u},\ \forall\, \boldsymbol{u}, \boldsymbol{v} \in \mathbb{R}^2$. The linearisation of A^P results in the equation

$$\begin{aligned} \frac{\Delta A^P}{A^P} &= \frac{1}{2A^P}\begin{bmatrix} \widetilde{\boldsymbol{y}_3^P - \boldsymbol{y}_2^P} & \widetilde{\boldsymbol{y}_1^P - \boldsymbol{y}_3^P} & \widetilde{\boldsymbol{y}_2^P - \boldsymbol{y}_1^P} \end{bmatrix}\begin{bmatrix} \Delta \boldsymbol{y}_1^P \\ \Delta \boldsymbol{y}_2^P \\ \Delta \boldsymbol{y}_3^P \end{bmatrix} = \\ &= \frac{1}{2A^P}\begin{bmatrix} \widetilde{\boldsymbol{y}_3^P - \boldsymbol{y}_2^P} & \widetilde{\boldsymbol{y}_1^P - \boldsymbol{y}_3^P} & \widetilde{\boldsymbol{y}_2^P - \boldsymbol{y}_1^P} \end{bmatrix}\begin{bmatrix} \boldsymbol{D}_1^P \\ \boldsymbol{D}_2^P \\ \boldsymbol{D}_3^P \end{bmatrix}\Delta \boldsymbol{Y} = \sum_{I=1}^{3}\left(\mathbf{J}_I^P \boldsymbol{D}_I^P\right)\Delta \boldsymbol{Y} \end{aligned} \tag{37}$$

where $\boldsymbol{J}_I^P = \epsilon_{IJK}\left(\widetilde{\boldsymbol{y}_K^P - \boldsymbol{y}_J^P}\right)/(4A^P), \quad I = 1, \ldots 3.$

6.1.3. Transformation from projected positions to global coordinates. The linearisations developed in the previous sections, were defined in terms of coordinates of the elements projected over the local plane $\boldsymbol{p}$. The nodal vector of increments in projected coordinates $\Delta \boldsymbol{Y}$ is locally defined in the plane, and consequently, must be computed in terms of $\Delta \boldsymbol{U}$, the vector global nodal coordinates of the contact elements defined in $\mathbb{R}^3$, Equation (17). To carry out this process, starting from Equation (16), the linearisation results in the following equation

$$\Delta \boldsymbol{y}_A^\alpha = \begin{bmatrix} \Delta \boldsymbol{e}_1 \cdot \left(\boldsymbol{x}_A^\alpha - \boldsymbol{x}_1^1\right) + \boldsymbol{e}_1 \cdot \Delta \boldsymbol{x}_A^\alpha - \boldsymbol{e}_1 \cdot \Delta \boldsymbol{x}_1^1 \\ \Delta \boldsymbol{e}_2 \cdot \left(\boldsymbol{x}_A^\alpha - \boldsymbol{x}_1^1\right) + \boldsymbol{e}_2 \cdot \Delta \boldsymbol{x}_A^\alpha - \boldsymbol{e}_2 \cdot \Delta \boldsymbol{x}_1^1 \end{bmatrix} = \boldsymbol{H}_A^\alpha \Delta \boldsymbol{U}, \tag{38}$$

where $\boldsymbol{H}_A^\alpha$ is a matrix which transforms the increments of local nodal coordinates into the global coordinates in $\mathbb{R}^3$. The full expression of matrix $\boldsymbol{H}_A^\alpha$ is outlined in the Appendix. Grouping the expressions for all nodes, we get

$$\Delta \boldsymbol{Y} = \boldsymbol{H}^\alpha \Delta \boldsymbol{U} \tag{39}$$

where $\boldsymbol{H}^\alpha$ is the matrix formed by joining together matrices $\boldsymbol{H}_A^\alpha$.

6.1.4. Final expression of weight factors linearisation. The linearisation of the weight factors is computed with Equations (26), (35) and (37), and given by

$$\Delta n_{AB}^{\alpha,P} = \boldsymbol{Q}_{AB}^{\alpha,P} \Delta \boldsymbol{Y} = \boldsymbol{Q}_{AB}^{\alpha,P} \boldsymbol{H}^\alpha \Delta \boldsymbol{U}, \qquad \alpha = 1, 2;\ \ A = 1, n^1;\ \ B = 1, m^\alpha \tag{40}$$

where

$$\boldsymbol{Q}_{AB}^{\alpha,P} = \sum_{g=1}^{n_g}\left[N_B^\alpha\left(\boldsymbol{\xi}_g^\alpha\right)\ \boldsymbol{P}_A^{1,P}\left(\boldsymbol{\xi}_g^1\right) + N_A^1\left(\boldsymbol{\xi}_g^1\right)\boldsymbol{P}_B^{\alpha,P}\left(\boldsymbol{\xi}_g^\alpha\right)\right] w_g A^P + n_{AB}^{\alpha,P}\sum_{I=1}^{3}\boldsymbol{J}_I^P \boldsymbol{D}_I^P, \tag{41}$$

is a row vector of $2m^1 + 2m^2$ components. The final expression of the linearisation of the weight factors is computed by adding up all contributions from the triangles in which the intersection area is subdivided:

$$\Delta n_{AB}^\alpha = \sum_P \Delta n_{AB}^{\alpha,P} = \boldsymbol{Q}_{AB}^\alpha \boldsymbol{H}^\alpha \Delta \boldsymbol{U} \tag{42}$$

with:

$$\boldsymbol{Q}_{AB}^\alpha = \sum_P \boldsymbol{Q}_{AB}^{\alpha,P}$$

DOI: 10.1002/nme

6.2. *Normal interpenetration linearisation*

The linearisation of the interpenetration $\boldsymbol{g}_A$, Equation (5), is given by

$$\Delta \boldsymbol{g}_A = \sum_{B=1}^{m^1} \left(n^1_{AB} \Delta \boldsymbol{x}^1_B + \Delta n^1_{AB} \boldsymbol{x}^1_B \right) - \sum_{C=1}^{m^2} \left(n^2_{AC} \Delta \boldsymbol{x}^2_C + \Delta n^2_{AC} \boldsymbol{x}^2_C \right). \tag{43}$$

Using Equation (43) and Equations (40 and 41) we get

$$\Delta \boldsymbol{g}_A = \boldsymbol{N}_A \Delta \boldsymbol{U}, \tag{44}$$

where

$$\begin{aligned} \boldsymbol{N}_A = & \left[N^1_1 \boldsymbol{I} \quad N^1_2 \boldsymbol{I} \quad \dots \quad N^1_{m^1} \boldsymbol{I} \quad -N^2_1 \boldsymbol{I} \quad -N^2_2 \boldsymbol{I} \quad \dots \quad -N^2_{m^2} \boldsymbol{I} \right] \\ & + \sum_{B=1}^{m^1} \left(\boldsymbol{x}^1_B \boldsymbol{Q}^1_{AB} \right) \boldsymbol{H}^1 - \sum_{C=1}^{m^2} \left(\boldsymbol{x}^2_C \boldsymbol{Q}^2_{AC} \right) \boldsymbol{H}^2. \end{aligned} \tag{45}$$

The linearisation of the normal interpenetration is then given by

$$\Delta g_{NA} = \boldsymbol{\nu}^T_A \boldsymbol{N}_A \Delta \boldsymbol{U} \tag{46}$$

6.3. *Linearisation of the normal vector*

To assure a quadratic convergence of the residual, the linearisation of the normal vector in the tangent stiffness matrix is required. The linearisation of Equation (24) yields

$$\Delta \boldsymbol{\nu}_A = \frac{[\boldsymbol{I} - \boldsymbol{\nu}_A \otimes \boldsymbol{\nu}_A]}{\| \boldsymbol{v}_A \times \boldsymbol{w}_A \|} \left[\; \widetilde{\boldsymbol{w}}_A \quad \widetilde{\boldsymbol{v}}_A - \widetilde{\boldsymbol{w}}_A \quad -\widetilde{\boldsymbol{v}}_A \; \right] \begin{bmatrix} \Delta \boldsymbol{x}^1_J \\ \Delta \boldsymbol{x}^1_A \\ \Delta \boldsymbol{x}^1_K \end{bmatrix}, \tag{47}$$

where

$$J = \operatorname{mod}(A, m^1) + 1, \qquad K = \operatorname{mod}(A+1, m^1) + 1, \qquad A = 1, \dots m^1.$$

After some algebra, Equation (47) can be written in the form

$$\Delta \boldsymbol{\nu}_A = \boldsymbol{W}_A \Delta \boldsymbol{U} \tag{48}$$

where matrix $\boldsymbol{W}_A$ is built taking into account the permutations described above.

6.4. *Tangent stiffness of the contact element*

After replacing Equations (42), (46) and (48) into Equation (25), the expression of the tangent stiffness of the contact element is obtained :

$$\begin{aligned} \delta \boldsymbol{\Phi}^e \cdot \boldsymbol{K}^e_{\text{cont}} \Delta \boldsymbol{\Phi}^e = & \sum_{A=1}^{m^1} \begin{bmatrix} \delta \boldsymbol{x}^1_B \\ \delta \boldsymbol{x}^2_C \\ \delta p_B \end{bmatrix} \\ & \times \begin{cases} \begin{bmatrix} \begin{gathered} \eta_A \left(\boldsymbol{\nu}_A \, \boldsymbol{Q}^1_{AB} \boldsymbol{H}^1 + n^1_{AB} \boldsymbol{W}_A \right) \\ + r n^1_{AB} [\boldsymbol{\nu}_A \otimes \boldsymbol{\nu}_A] \boldsymbol{N}_A \end{gathered} & k n^1_{AB} \boldsymbol{\nu}_A \\ \begin{gathered} -\eta_A \left(\boldsymbol{\nu}_A \, \boldsymbol{Q}^2_{AC} \boldsymbol{H}^2 + n^1_{AC} \boldsymbol{W}_A \right) \\ - r n^2_{AC} [\boldsymbol{\nu}_A \otimes \boldsymbol{\nu}_A] \boldsymbol{N}_A \end{gathered} & k n^2_{AC} \boldsymbol{\nu}_A \\ \boldsymbol{\delta}_{AB} k \boldsymbol{\nu}^T_A \boldsymbol{N}_A & \boldsymbol{0} \end{bmatrix} \begin{bmatrix} \Delta \boldsymbol{U} \\ \Delta p_A \end{bmatrix}, & \eta_A \leqslant 0 \\ \begin{bmatrix} \boldsymbol{0} & \boldsymbol{0} \\ \boldsymbol{0} & \boldsymbol{0} \\ \boldsymbol{0} & -\frac{k^2}{r} \boldsymbol{\delta}_{AB} \end{bmatrix} \begin{bmatrix} \Delta \boldsymbol{U} \\ \Delta p_A \end{bmatrix}, & \eta_A > 0. \end{cases} \end{aligned} \tag{49}$$

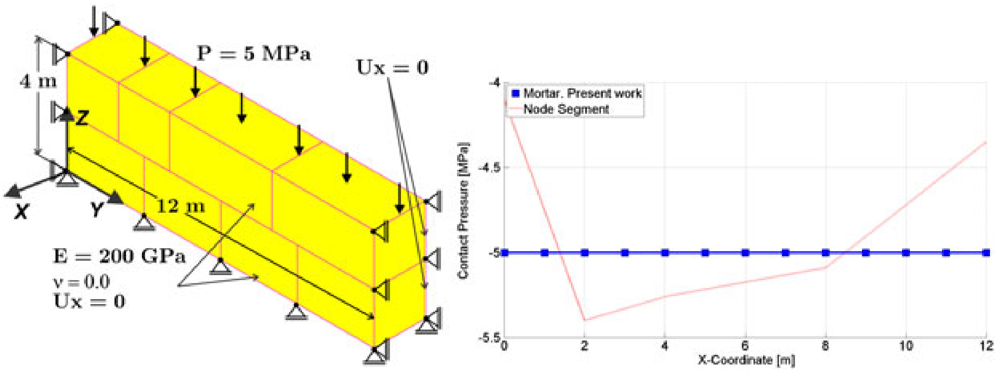

(a) (b)

Figure 3. Contact patch test. (a) Boundary conditions and mechanical properties. (b) Stress solution of the node-segment and mortar algorithms in the contact interface.

7. NUMERICAL EXAMPLES

Five numerical examples are presented to evaluate the robustness and accuracy of the proposed contact algorithm. The examples involve quasi-static simulations and were carried-out in the research finite element code Oofelie [40] where the contact algorithm is integrated. All pre-processing and post-processing tasks were performed using the software SAMCEF-Field [41].

7.1. *Validation example I. The contact patch test*

The first example is a contact patch test proposed by Chen and Hisada [42]. The 3D solutions obtained in this work are compared with the 2D solutions of Chen and Hisada, introducing a plane strain state, which reproduces the same boundary conditions. The material behaviour used in this example is linear elastic. The mesh topology, boundary conditions, dimensions and material properties are shown in Figure 3(a).

Figure 3(b) shows that the stress field is transmitted exactly from one body to the other with nonconforming meshes, concluding that the formulation verifies the contact patch test to machine accuracy. When using a node–segment approach, the stress field is not uniform, and thus, does not pass the contact patch test (Figure 3(b)).

In order to study the influence of the parameters r and k on the convergence properties, solutions for different values of r and k were computed. From the geometry and material properties depicted in Figure 3, and by using the Equation (14), their recommended value results as follows:

$$r = k = 10\frac{E}{h} = 10\frac{2.1\times 10^{9}}{2} = 1.05\times 10^{10} \tag{50}$$

Table I gives the residual norm per iteration for the different values of r and k. Quadratic convergence behaviour is displayed in almost all cases. The optimal behaviour is achieved when they are calculated by using Equation (14). The condition number of the global tangent matrix is shown in Table II. We see that the minimum condition number is obtained for values of r and k close to values suggested by Equation (14). In the examples that follow, coefficients r and k are selected according to Equation (14).

7.2. *Validation example II. Hertzian contact*

The second example, the Hertz contact problem between two parallel cylinders [9,43], was selected to validate the algorithm with an analytic solution. The radius of both cylinders is 8. The mesh topology, boundary conditions and mechanical properties are shown in Figure 4. A nonconforming mesh in the contact interface of the cylinders is proposed. Symmetry conditions with respect to

DOI: 10.1002/nme

Table I. Residual norm evolution in the contact patch test problem for different values of k and r ($r = k$).

Iteration	10^6	10^8	10^{10}	10^{12}	10^{14}
1	1.42×10^{-2}	3.35×10^{-1}	10.2751	84.1781	5.43×10^3
2	3.07×10^{-1}	4.84×10^{-2}	7.80×10^{-2}	6.99×10^{-1}	9.14×10^1
3	1.75×10^{-3}	7.39×10^{-3}	3.89×10^{-6}	1.07×10^{-3}	3.37×10^3
4	1.24×10^{-4}	7.78×10^{-5}		1.39×10^{-9}	2.77×10^1
5	3.77×10^{-11}	2.18×10^{-11}			1.93×10^3
6					1.24×10^2
7					8.32×10^2
8					3.84×10^5
9					Fail

Table II. Condition of the tangent matrix for the contact patch test problem for different values of k and r.

$r \setminus k$	10^6	10^8	10^{10}	10^{12}	10^{14}
10^6	1.22×10^8	1.22×10^4	1.16×10^2	1.12×10^4	1.12×10^6
10^8	1.27×10^8	1.27×10^4	1.17×10^2	1.12×10^4	1.12×10^6
10^{10}	2.21×10^9	2.21×10^5	2.38×10^2	1.12×10^4	1.11×10^6
10^{12}	8.27×10^{12}	8.27×10^8	8.28×10^4	2.40×10^4	1.09×10^6
10^{14}	∞	∞	∞	∞	∞

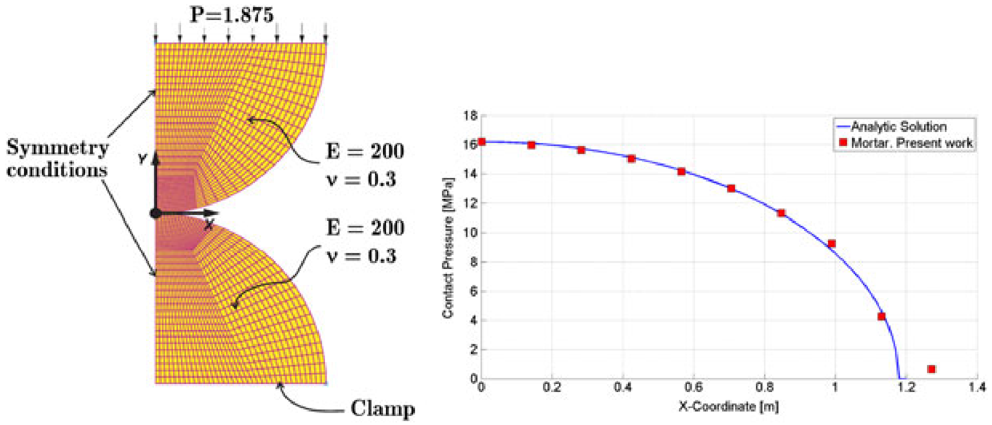

(a) (b)

Figure 4. Hertz contact of two parallel cylinders. (a) Boundary conditions and mechanical properties. (b) Hertz contact stress solution using nonconforming mesh.

a middle plane are selected to reduce the computational cost, allowing the mesh to be refined at the contact surface. The upper cylinder is uniformly pressed with a small pressure value, leading to small strains. Figure 4(b) shows the variation of contact pressure at the contact zone, showing agreement between the analytical solution from Hertz theory and the proposed numerical solution using the mortar method.

7.3. *Ironing problem*

The third example, depicted in Figure 5, corresponds to the so-called ironing problem. It was presented in the work of Puso *et al.* [9] and solved by a mortar based contact formulation with a penalty regularisation scheme. In the work of Popp *et al.* [26], this example is solved by a dual mortar approach with Lagrange multipliers.

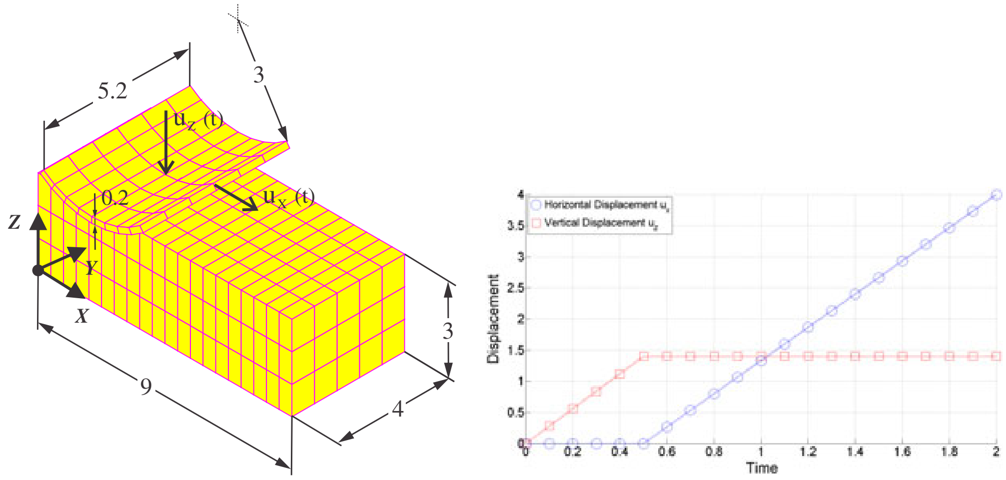

(a) (b)

Figure 5. Ironing example. (a) Geometry, mesh discretisation and boundary conditions. (b) Time evolution of imposed displacements of die.

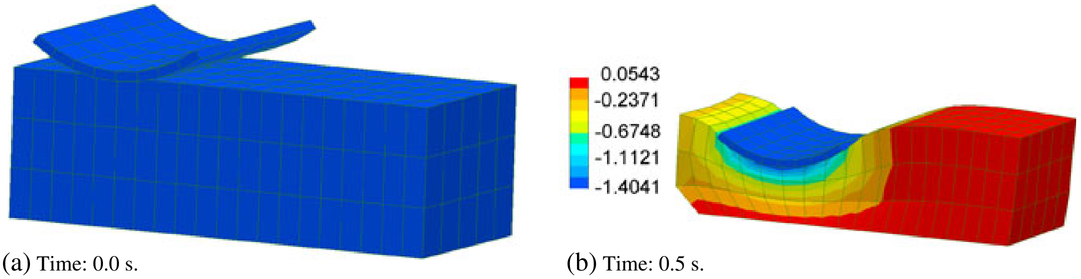

(a) Time: 0.0 s. (b) Time: 0.5 s.

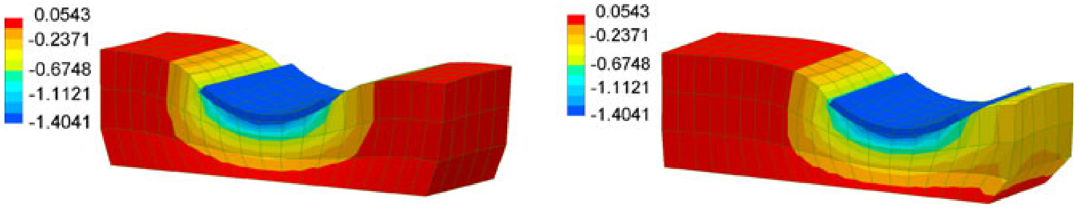

(c) Time: 1.39 s. (d) Time: 2 s.

Figure 6. Ironing example. Plot of displacements computed at four different time instants.

A cylindrical die with $E = 1000$ and $\nu = 0.3$, is pressed into an elastic block with $E = 1000$ and $\nu = 0.499$. For simplicity, a linear elastic material is assumed. The discretisation is performed using eight-nodes hexahedral finite elements.

The displacement of the top surface of the cylindrical die is imposed, as shown in Figure 5(b). First, the die is moved vertically downwards from time 0 to time 0.5 s, and then it is displaced horizontally from time 0.5 s up to time 2 s.

Computations are performed with a constant time-step of 0.01 s. Figure 6 shows the deformation at four time instants, illustrating the large displacements involved in the example. Figure 7(a) shows the vertical stress σ_z at the outer surface of the slab. The computed stresses are smooth, without jumps or oscillations between elements. Figure 7(b) shows the evolution in time of the vertical component of stress σ_z on the slab surface, evaluated at a point located immediately below the centre of the die. Only a very slight oscillation of stress is evident, when the die slides along the slab, and is

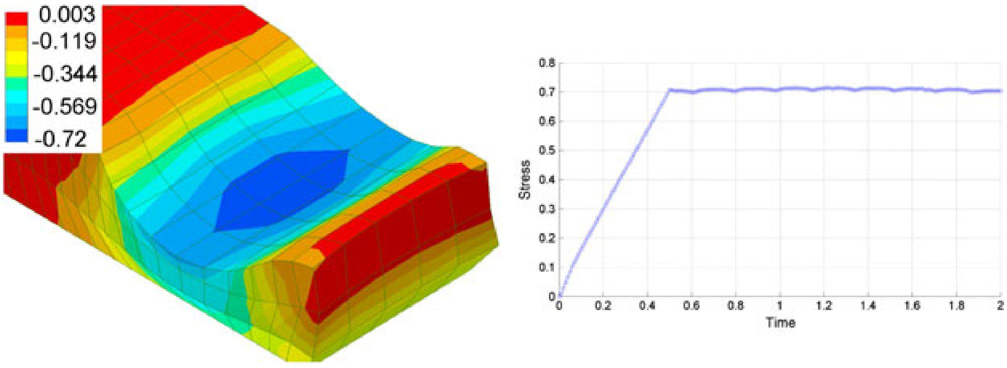

(a) (b)

Figure 7. Ironing example. Computed stress solutions. (a) Stress σ_z computed at the external surface of the slab. (b) Stress σ_z computed on the slab surface at a point below the center of the die.

Table III. Residual norm evolution for the ironing example for different times.

Iteration	Time 0.5 (s)	Time 0.98 (s)	Time 1.94 (s)
1	6.09×10^{-2}	9.73×10^{-2}	1.37
2	7.34×10^{-4}	9.55×10^{-4}	1.11×10^{-3}
3	2.65×10^{-4}	3.80×10^{-4}	3.39×10^{-4}
4	6.35×10^{-5}	1.00×10^{-4}	9.01×10^{-5}
5	6.57×10^{-8}	3.50×10^{-5}	6.24×10^{-9}
6		4.87×10^{-9}	

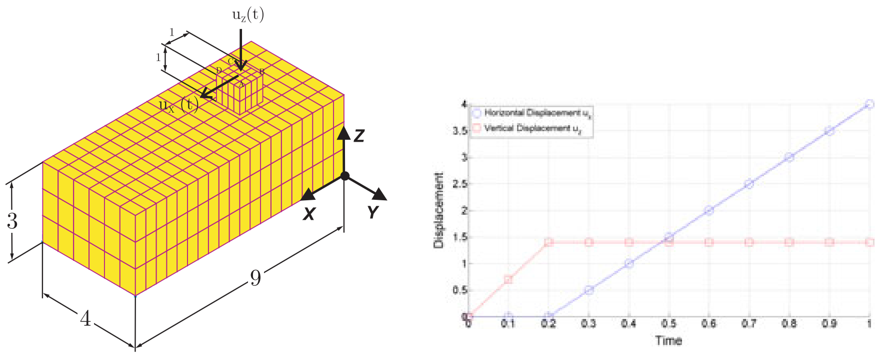

(a) (b)

Figure 8. Indenter example. (a) Geometry, mesh discretisation and boundary conditions. (b) Time evolution of exposed displacements of die.

produced by the finite element discretisation. A quadratic converge was obtained with six iterations per step.

Table III presents the convergence rate for three representative time steps (Figure 5)(b)). By using an appropriate value of coefficients r and k, selected according to Equation (14), which gives in this case $r = k = 11$, the convergence rate is quadratic with a mean value of six iterations per step, see Table III.

7.4. Indenter problem

A fourth example, the so-called indenter, depicted in Figure 8, is analysed in this section [9, 26]. A cubic upper block ($E = 1000$ and $\nu = 0.3$) is pressed into a slab ($E = 1$ and $\nu = 0.3$),

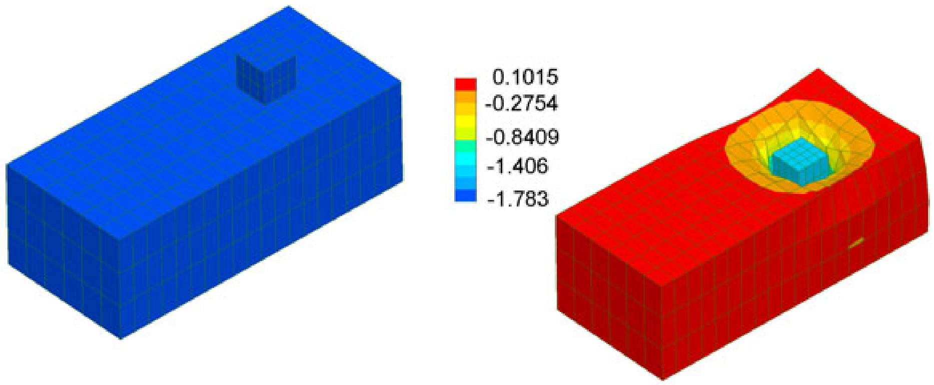

(a) Time: 0.0 s. (b) Time: 0.2 s.

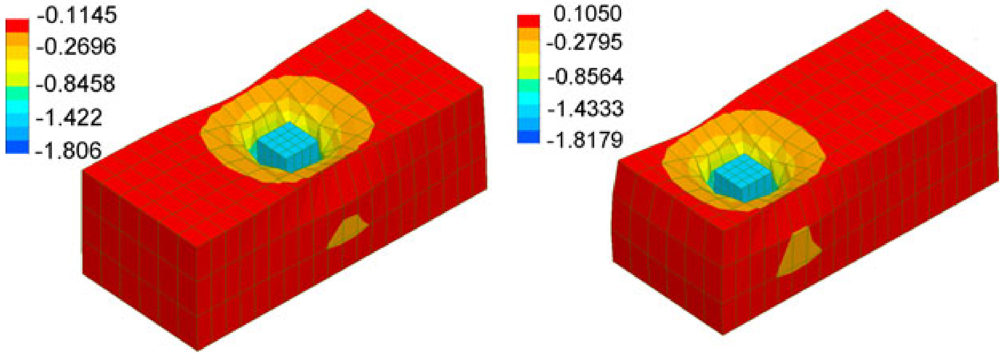

(c) Time: 0.66 s. (d) Time: 1 s.

Figure 9. Indenter example. True deformation solutions for different time instants.

and then made to slide over the slab surface. A linear elastic constitutive law is again assumed. This example is more challenging than the previous one because of the sharp corners of the upper block, which produce very large contact pressures. Dimensions, mesh topology and boundary conditions are shown in Figure 8. The displacement of the top surface of the upper block is imposed, as shown in Figure 8(b). First, the block is moved downwards vertically from time 0 to 0.2 s, and then it is displaced horizontally from time 0.2 s up to time 1 s. A classical node-to-segment approach and a smooth node–segment contact approach have failed to obtain a solution in this example [9].

Figure 9 shows the computed solutions in four time instants.

Figure 10(a) shows the computed vertical stress σ_z at the outer surface of the slab for time 0.83 s. The computed stresses are smooth, without jumps or oscillations between elements. Figure 10(b) shows the evolution in time of the vertical component of stress σ_z on the slab surface, evaluated at a point located immediately below the centre of the upper block. An almost constant stress value is observed, with smooth oscillations because of the discretisation.

Table IV presents the convergence rate for three representative time steps, see Figure (10)(b). By using an appropriate value of coefficients r and k, selected according to Equation (14), which gives in this case $r = k = 100$, the convergence rate is quadratic with a mean value of four iterations per step, see Table IV. Computations are performed with a constant time-step of 0.01 s.

7.5. Application example: internal combustion engine valve

The fifth example corresponds to the case of an industrial application, the contact between an internal combustion engine valve with its seat (Figure 11(a)). A more detailed explanation of the characteristics of this mechanical component can be found in [44]. This problem is challenging because of the small contact surfaces with double curvature.

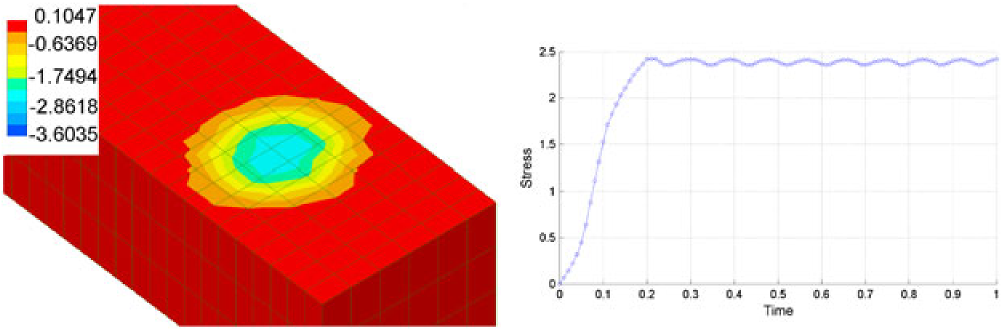

(a) (b)

Figure 10. Indenter example. Plots of computed stress. (a) Stress σ_z computed at the external surface of the slab. (b) Stress σ_z computed on the slab surface at a point below the center of the upper block.

Table IV. Residual norm evolution for the indenter example for different times.

Iteration	Time 0.2 (s)	Time 0.5 (s)	Time 2 (s)
1	1.90	1.90	1.90
2	1.32×10^{-2}	1.22×10^{-2}	1.45×10^{-2}
3	3.76×10^{-4}	4.59×10^{-5}	6.15×10^{-4}
4	1.61×10^{-7}	8.75×10^{-8}	2.53×10^{-7}

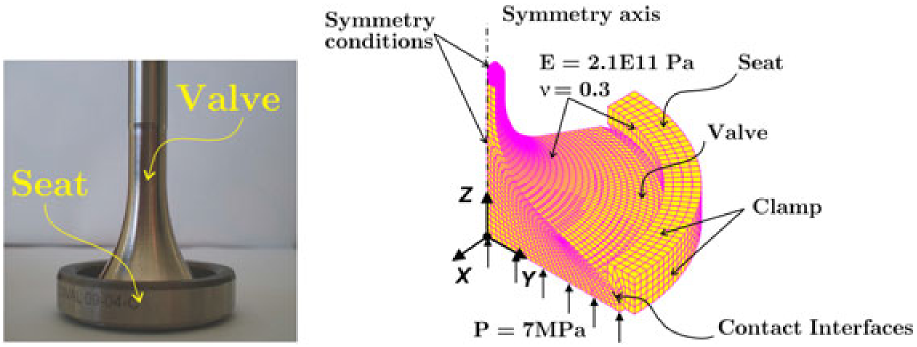

(a) (b)

Figure 11. Application example. (a) Contact between a combustion engine valve and its seat; (b) boundary conditions, mechanical properties and mesh topology for a combustion engine valve.

A constant pressure value of 7 MPa is applied at the head of the valve. This represents the internal pressure produced by the combustion in the cylinder. Linear elastic behaviour of the materials and small deformations are assumed. Figure 11(b) details the geometry, boundary conditions and mechanical properties used for the model proposed. The mesh topology consists of hexahedral elements.

Figure 12(a) shows the distribution of contact pressure obtained with the node-to-segment approach, whereas Figure 12(b) displays the solution computed with the mortar scheme. A large pressure oscillation is observed in the contact area when using a node-to-segment approach, whereas with the mortar method, the pressure distribution is much more uniform (Figure 12(b)). The cyclical behaviour in the computation of pressures with the node-to-segment scheme is caused by small perturbations in the mesh geometry. The mortar method is less sensitive to these errors because of the mixed approach in which efforts are translated between bodies by means of the contact pressure approximation.

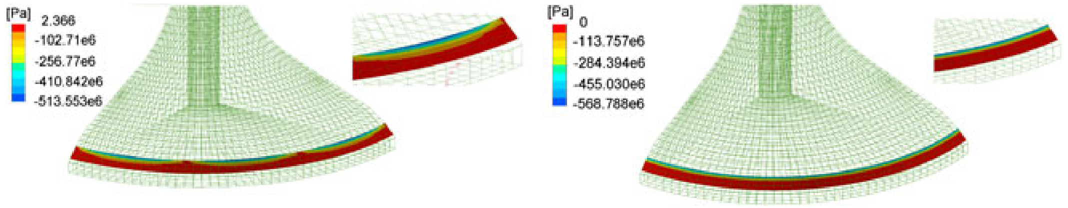

(a) (b)

Figure 12. Application example. Comparison of contact pressures computed with both approaches. (a) Node-to-segment approach and (b) mortar approach.

8. CONCLUSIONS

A new mortar finite element formulation combined with an augmented Lagrangian technique has been proposed for the solution of 3D frictionless contact problems. The algorithm has three main features: the nonlinear equations can be solved by means of a monolithic Newton scheme of simple implementation, problems with nonconforming meshes can be accurately solved, and the results do not depend on the definition of any penalty parameter by the users.

The equations for the computation of the residual forces and tangent matrices were presented. The strategy can be implemented very easily in a finite elements programme for nonlinear analysis without any change to the main structure of the code.

The numerical examples showed that the proposed strategy successfully passes the contact patch test. The technique was validated by comparison with a classic analytical solution. Two examples were presented to demonstrate the capabilities of our proposal to represent large displacements contact problems. Finally, an industrial application has been solved.

We emphasise the accurate pressure prediction at the contact surface obtained in all examples presented in this work. This feature is imperative to obtain reliable solutions in related computations, that is, when analysing wear between mechanical components. An extension of the method to cases with friction and wear is currently under development and will be reported in future work.

APPENDIX A: VARIATION OF THE NORMAL TO THE NON-MORTAR FACET

An orthonormal local basis $\{\boldsymbol{e}_1, \boldsymbol{e}_2, \boldsymbol{e}_3\}$ is defined for each non-mortar facet, in terms of the nodal coordinates $\boldsymbol{x}^1_A$. Vector $\boldsymbol{e}_3$ is normal to the facet in the case of a triangular facet ($m^1 = 3$), or normal to the plane defined by the two diagonals in the case of a quadrangular facet ($m^1 = 4$):

$$\boldsymbol{e}_3 = \frac{\left(\boldsymbol{x}^1_3 - \boldsymbol{x}^1_1\right) \times \left(\boldsymbol{x}^1_{m^1} - \boldsymbol{x}^1_2\right)}{\| \left(\boldsymbol{x}^1_3 - \boldsymbol{x}^1_1\right) \times \left(\boldsymbol{x}^1_{m^1} - \boldsymbol{x}^1_2\right) \|}. \tag{A.1}$$

Vector $\boldsymbol{e}_1$ is aligned with the line joining nodes 1 and 3:

$$\boldsymbol{e}_1 = \frac{\boldsymbol{x}^1_3 - \boldsymbol{x}^1_1}{\|\boldsymbol{x}^1_3 - \boldsymbol{x}^1_1\|}. \tag{A.2}$$

Finally, vector $\boldsymbol{e}_2$ is computed so as to get a right frame:

$$\boldsymbol{e}_2 = \boldsymbol{e}_3 \times \boldsymbol{e}_1. \tag{A.3}$$

The linearisation of vector $\boldsymbol{e}_1$ is obtained from Equation (A.2) as follows,

$$\Delta \boldsymbol{e}_1 = \mathbf{F}\left(\Delta \boldsymbol{x}^1_3 - \Delta \boldsymbol{x}^1_1\right), \tag{A.4}$$

being

$$\boldsymbol{F}=\frac{(\boldsymbol{I}-\boldsymbol{e}_1\otimes\boldsymbol{e}_1)}{\|\boldsymbol{x}_3^1-\boldsymbol{x}_1^1\|}. \tag{A.5}$$

The linearisation of Equation (A.1) is computed from

$$\Delta\boldsymbol{e}_3=\sum_{I=1,m_1}\boldsymbol{A}^I\Delta\boldsymbol{x}_I^1, \tag{A.6}$$

where the matrix $\boldsymbol{A}=\left[\begin{array}{cccc}\boldsymbol{A}^1 & \boldsymbol{A}^2 & \cdots & \boldsymbol{A}^{m_1}\end{array}\right]$ is given by

$$\boldsymbol{A}=\begin{cases}\dfrac{(\boldsymbol{I}-\boldsymbol{e}_3\otimes\boldsymbol{e}_3)}{\|\left(\boldsymbol{x}_3^1-\boldsymbol{x}_1^1\right)\times\left(\boldsymbol{x}_3^1-\boldsymbol{x}_2^1\right)\|}\left[\begin{array}{ccc}\widetilde{\left(\boldsymbol{x}_3^1-\boldsymbol{x}_2^1\right)} & \widetilde{\left(\boldsymbol{x}_1^1-\boldsymbol{x}_3^1\right)} & \widetilde{\left(\boldsymbol{x}_2^1-\boldsymbol{x}_1^1\right)}\end{array}\right], & m_1=3;\\[2ex] \dfrac{(\boldsymbol{I}-\boldsymbol{e}_3\otimes\boldsymbol{e}_3)}{\|\left(\boldsymbol{x}_3^1-\boldsymbol{x}_1^1\right)\times\left(\boldsymbol{x}_4^1-\boldsymbol{x}_2^1\right)\|}\left[\begin{array}{cccc}\widetilde{\left(\boldsymbol{x}_4^1-\boldsymbol{x}_2^1\right)} & \widetilde{\left(\boldsymbol{x}_1^1-\boldsymbol{x}_3^1\right)} & \widetilde{\left(\boldsymbol{x}_2^1-\boldsymbol{x}_4^1\right)} & \widetilde{\left(\boldsymbol{x}_3^1-\boldsymbol{x}_1^1\right)}\end{array}\right], & m_1=4.\end{cases} \tag{A.7}$$

The operator $\widetilde{\boldsymbol{u}}:\mathbb{R}^3\rightarrow\mathbb{R}^3\otimes\mathbb{R}^3$ returns a 3×3 skew-symmetric matrix such that $\boldsymbol{u}\times\boldsymbol{v}=\widetilde{\boldsymbol{u}}\boldsymbol{v}=-\boldsymbol{v}\times\boldsymbol{u},\ \forall\ \boldsymbol{u},\boldsymbol{v}\in\mathbb{R}^3$. The linearisation of the vector $\boldsymbol{e}_2$ is obtained from Equation (A.3)

$$\Delta\boldsymbol{e}_2=\widetilde{\boldsymbol{e}}_3\Delta\boldsymbol{e}_1-\widetilde{\boldsymbol{e}}_1\Delta\boldsymbol{e}_3, \tag{A.8}$$

where $\widetilde{\boldsymbol{e}}_3$ and $\widetilde{\boldsymbol{e}}_1$ are the skew matrices associated to the vectors $\boldsymbol{e}_3$ and $\boldsymbol{e}_1$, respectively.

The linearisation of the projected positions of the two facets on the computation plane was given in Equation (38). After replacing Equations (A.4) and (A.8) in the latter, we get the following:

$$\Delta\boldsymbol{y}_A^\alpha=\boldsymbol{H}_A^\alpha\Delta\boldsymbol{U}. \tag{A.9}$$

Matrix $\boldsymbol{H}_A^\alpha$ is a $2\times 3(m_1+m_2)$ matrix given by

$$\begin{aligned}\boldsymbol{H}_A^\alpha=\boldsymbol{X}_A^\alpha&\left[\begin{array}{cccccccc}-\boldsymbol{F} & \boldsymbol{0} & \boldsymbol{F} & \boldsymbol{0} & \boldsymbol{0} & \boldsymbol{0} & \ldots\\ -\widetilde{\boldsymbol{e}}_1\boldsymbol{A}^1+\widetilde{\boldsymbol{e}}_3\boldsymbol{F} & -\widetilde{\boldsymbol{e}}_1\boldsymbol{A}^2 & -\widetilde{\boldsymbol{e}}_1\boldsymbol{A}^3+\widetilde{\boldsymbol{e}}_3\boldsymbol{F} & -\widetilde{\boldsymbol{e}}_1\boldsymbol{A}^4 & \boldsymbol{0} & \boldsymbol{0} & \ldots\end{array}\right]\\ &+\begin{array}{c}\left[\begin{array}{cccccc}\boldsymbol{e}_1^T & \boldsymbol{0}^T & \ldots & -\boldsymbol{e}_1^T & \boldsymbol{0} & \ldots\\ \boldsymbol{e}_2^T & \boldsymbol{0}^T & \ldots & -\boldsymbol{e}_2^T & \boldsymbol{0} & \ldots\end{array}\right]\\ \qquad\qquad\uparrow\\ \qquad\qquad A,\alpha\end{array}\end{aligned} \tag{A.10}$$

where in the last matrix of the right-hand-side, entry $\left[\begin{array}{c}-\boldsymbol{e}_1^T\\ -\boldsymbol{e}_2^T\end{array}\right]$ is added at the column corresponding to node A,α, and where

$$\boldsymbol{X}_A^\alpha=\left[\begin{array}{cc}\left(\boldsymbol{x}_A^\alpha-\boldsymbol{x}_1^1\right)^T & \boldsymbol{0}^T\\ \boldsymbol{0}^T & \left(\boldsymbol{x}_A^\alpha-\boldsymbol{x}_1^1\right)^T\end{array}\right] \tag{A.11}$$

APPENDIX B: SEGMENT INTERSECTION

The segment intersections used to generate the intersection polygon in $\mathbb{R}^2$ were made using an algorithm based on rules of advancing, as proposed by O'Rourke [37]. The segments $\overline{\boldsymbol{ab}}$ and $\overline{\boldsymbol{cd}}$ are defined by $\overline{\boldsymbol{ab}}=\boldsymbol{a}-\boldsymbol{b}$ and $\overline{\boldsymbol{cd}}=\boldsymbol{c}-\boldsymbol{d}$ (Figure B.1). The position $\boldsymbol{P}_{\mathrm{int}}(t)\equiv\boldsymbol{Q}_{\mathrm{int}}(s)$ of the intersection point between $\overline{\boldsymbol{ab}}$ and $\overline{\boldsymbol{cd}}$ is calculated using the parametric representation of a segment,

$$\boldsymbol{Q}_{\mathrm{int}}(s)=\boldsymbol{a}+s(\boldsymbol{b}-\boldsymbol{a}), \tag{B.1}$$

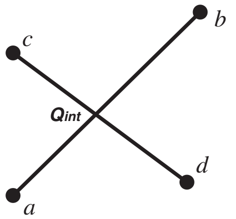

Figure B.1. Segment intersection.

or

$$\boldsymbol{P}_{\text{int}}(t) = \boldsymbol{c} + t(\boldsymbol{d} - \boldsymbol{c}), \tag{B.2}$$

where the scalar variables s and t are the *parameters* along each segment. Parameter values s and t are computed by making $\boldsymbol{P}_{\text{int}}(t)$ equal to $\boldsymbol{Q}_{\text{int}}(s)$, giving a system of two equations with two unknowns with the following solution:

$$\begin{aligned} s &= [a_x(d_y - c_y) + c_x(a_y - d_y) + d_x(c_y - a_y)]/D, \\ t &= [a_x(c_y - b_y) + b_x(a_y - c_y) + c_x(b_y - a_y)]/D, \\ \text{with} \quad D &= a_x(d_y - c_y) + b_x(c_y - d_y) + d_x(b_y - a_y) + c_x(a_y - b_y). \end{aligned} \tag{B.3}$$

The linearisation of Equation (A.11) is straightforward resulting in the following generic equation:

$$\Delta \boldsymbol{Q}_{\text{int}} = \bar{\bar{\boldsymbol{Q}}} \cdot \begin{bmatrix} \Delta \boldsymbol{a} \\ \Delta \boldsymbol{b} \\ \Delta \boldsymbol{c} \\ \Delta \boldsymbol{d} \end{bmatrix}, \tag{B.4}$$

where the matrix $\bar{\bar{\boldsymbol{Q}}}$ is a function of the segment points $\boldsymbol{a}$, $\boldsymbol{b}$, $\boldsymbol{c}$ and $\boldsymbol{d}$.

The matrix $\boldsymbol{D}_I^P$

The matrix $\boldsymbol{D}_I^P$ relates the nodal coordinate variation of a non-mortar or a mortar element of each triangle P with the nodal coordinate variation,

$$\Delta \boldsymbol{y}_I^P = \boldsymbol{D}_I^P \Delta \hat{\boldsymbol{\Phi}}_{KL}. \tag{B.5}$$

The geometric centre variation of the polygon $\mathcal{P}$ can be written with the average of the vertex of $\mathcal{P}$

$$\Delta \boldsymbol{y}_c^P = \frac{1}{n^P} \sum_{P=1}^{n^P} \Delta \boldsymbol{y}_I^P \qquad I = 1 \ldots 3. \tag{B.6}$$

where $\Delta \boldsymbol{y}_I^P$ is the variation of a vertex I for each triangle P (Figure B.2).

The matrix $\boldsymbol{D}_I^P$ depends directly on the intersection of the non-mortar $\tilde{k}$ and mortar $\tilde{l}$ elements. The simplest situation occurs when a vertex of a triangle P is coincident with a node of a non-mortar $\tilde{k}$ or mortar $\tilde{l}$ element. In this case, $\boldsymbol{D}_I^P$ will be formed by ones and zeros in the rows and columns corresponding to the DOFs of the vertex $\boldsymbol{y}_i^\alpha$. This case is presented in Figure B.2, where the node of the triangle P is coincident with the mortar node $\boldsymbol{y}_2^2$. A more complex situation arises when the intersection between $\tilde{k}$ and $\tilde{l}$ defines a vertex of the triangle P, it is $\boldsymbol{y}_{\text{int}}^P$. This situation, for example, is given by the segments intersection $\overline{\boldsymbol{y}_3^2 - \boldsymbol{y}_2^2}$ and $\overline{\boldsymbol{y}_4^1 - \boldsymbol{y}_3^1}$ (Figure B.2). In this case, $\boldsymbol{D}_I^P$ will be formed with the values coming from the matrix $\bar{\bar{\boldsymbol{Q}}}$, Equation (B.4).

DOI: 10.1002/nme

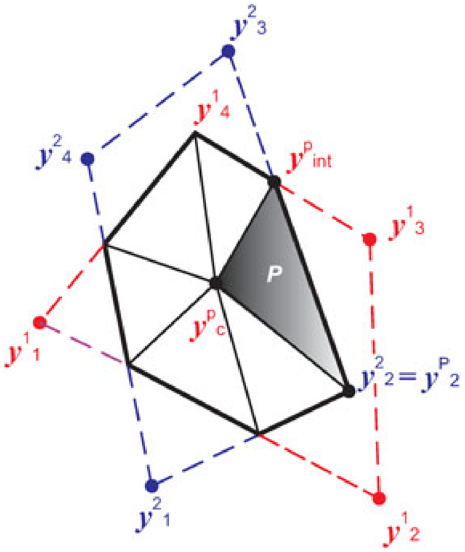

Figure B.2. Mortar and non-mortar element projected in the plane $\boldsymbol{p}$.

ACKNOWLEDGEMENTS

This work has received financial support from Consejo Nacional de Investigaciones Científicas y Técnicas (CONICET), Agencia Nacional de Promoción Científica y Tecnológica (ANPCyT) and Universidad Nacional del Litoral. Comments by reviewers are gratefully acknowledged.

REFERENCES

1. Gamez-Montero P, Zárate F, Sánchez M, Castilla R, Codina E. El problema del contacto en bombas de engranajes de perfil troncoidal. *Métodos numéricos para el calculo y diseño de ingeniería* 2005; **21**:213–229.
2. Bathe K. On the state of finite element procedures for forming processes. In *Proceedings of the NUMIFOR'04, Material Processing and Design: Modeling, Simulation and Applications*, Glosh S (ed.). American Institute of Physics: Melville, 2004; 34.
3. Madge J, Leen S, McColl I, Shipway P. Contact-evolution based prediction of fretting fatigue life: effect of slip amplitude. *Wear* 2007; **262**:1159–1170.
4. Wriggers P. *Computational Contact Mechanics*. John Wiley and Sons: Chichester, 2002.
5. Laursen T. *Computational Contact and Impact Mechanics*. Springer: Berlin, Heidelberg, 2002.
6. Parisch H. A consistent tangent stiffness matrix for three-dimensional non-linear contact analysis. *International Journal for Numerical Methods in Engineering* 1989; **28**:1803–1812.
7. Papadopoulos P, Taylor R. A mixed formulation for the finite element solution of contact problems. *Technical Report UCB/ SEMM Report 90/18*, University of California at Berkeley, 1990.
8. El-Abbasi N, Meguid S, Czekanski A. On the modelling of smooth contact surfaces using cubic splines. *International Journal for Numerical Methods in Engineering* 2001; **50**:953–967.
9. Puso M, Laursen T. A mortar segment-to-segment contact method for large deformation solid mechanics. *Computer Methods in Applied Mechanics and Engineering* 2004; **193**:601–629.
10. EI-Abbasi N, Bathe K. Stability and patch test performance of contact discretizations and a new solution algorithm. *Computer and Structures* 2001; **79**:1473–1486.
11. Oliveira M, Alves J, Menezes L. Algorithms and strategies for treatment of large deformation frictional contact in the numerical simulation of deep drawing process. *Archives of Computational Methods in Engineering: State of the Art Reviews* 2008; **15**:113–162.
12. Wohlmuth B. *Discretization Methods and Iterative Solvers Based on Domain Descomposition*. Springer: Berlin, 2001.
13. Dohrmann C, Key S, Heinstein M. Methods for connecting dissimilar three-dimensional finite element meshes. *International Journal for Numerical Methods in Engineering* 2000; **47**:1057–1080.
14. Kim C, Lazarov R, Pasciak J, Vassilevski P. Multiplier spaces for the mortar finite element method in three dimensions. *SIAM Journal on Numerical Analysis* 2000; **38**:519–538.
15. Belgacem F, Maday Y. A spectral element methodology tuned to parallel implementations. *Computer Methods in Applied Mechanics and Engineering* 1994; **116**:59–67.

16. Bernardi C, Maday Y, Patera A. A new nonconforming approach to domain decomposition: the mortar element method. In *Nonlinear Partial Differential Equations and Their Applications*, Brezis H, Lions J (eds). Pitman: London, 1992; 13–51.
17. Puso M, Laursen T, Solberg J. A segment-to-segment mortar contact method for quadratic elements and large deformations. *Computer Methods in Applied Mechanics and Engineering* 2008; **197**:555–566.
18. Puso M, Laursen T. A mortar segment-to-segment frictional contact method for large deformations. *Computer Methods in Applied Mechanics and Engineering* 2004; **193**:4891–4913.
19. Puso M. A 3D mortar method for solid mechanics. *International Journal for Numerical Methods in Engineering* 2004; **59**:315–336.
20. Bertsekas D. *Constrained Optimization and Lagrange Multiplier Methods*. Academic Press: New York, 1984.
21. Hestenes M. Multiplier and gradient methods. *Journal of Optimization Theory and Applications* 1969; **4**:303–320.
22. Powell M. A method for nonlinear constraints in optimization problems. In *Optimization*, Fletcher R (ed.). Academic Press: London, 1969; 283–298.
23. Rockafellar R. Augmented Lagrangians and applications of the proximal point algorithm in convex programming. *Mathematics of Operations Research* 1976; **1**:97–116.
24. Yang B, Laursen T, Meng X. Two-dimensional mortar contact methods for large deformation frictional sliding. *International Journal for Numerical Methods in Engineering* 2005; **62**:1183–1225.
25. Wohlmuth B. A mortar finite element method using dual spaces for the Lagrange multiplier. *SIAM Journal on Numerical Analysis* 2000; **38**(3):989–1012.
26. Popp A, Gitterle M, Gee MW, Wall WA. A dual mortar approach for 3D finite deformation contact with consistent linearization. *International Journal for Numerical Methods in Engineering* 2010; **83**:1428–1465.
27. Alart P, Curnier A. A mixed formulation for frictional contact problems prone to Newton like solution methods. *Computer Methods in Applied Mechanics and Engineering* 1991; **92**:353–375.
28. Christensen P, Klarbring A, Pang J, Stromberg N. Formulation and comparison of algorithms for frictional contact problems. *International Journal for Numerical Methods in Engineering* 1998; **42**:145–173.
29. Christensen P. A semi-smooth Newton method for elasto-plastic contact problems. *International Journal of Solids and Structures* 2002; **39**:2323–2341.
30. Hueber S. Discretization techniques and efficient algorithms for contact problems. *Ph.D. Thesis*, Universitat Stuttgart, 2008.
31. Hueber S, Stadler G, Wohlmuth B. A primal-dual active set algorithm for three-dimensional contact problems with Coulomb friction. *SIAM* 2008; **30**:572–596.
32. Gitterle M, Popp A, Gee M, Wall W. Finite deformation frictional mortar contact using a semi-smooth Newton method with consistent linearization. *International Journal for Numerical Methods in Engineering* 2010; **84**:543–571.
33. Hager C, Wohlmuth B. Nonlinear complementary functions for plasticity problems with frictional contact. *Computer Methods in Applied Mechanics and Engineering* 2009; **198**:3411–3427.
34. Cavalieri F, Cardona A. Contact modelling using an augmented Lagrangian technique and a mortar algorithm. In *In CD-ROM Proceedings Multibody Dynamics 2011, ECCOMAS Thematic Conference*, Samin J, Fisette P (eds). ECCOMAS: Brussels, Belgium, 2011; 1–18.
35. De Lorenzis L, Wriggers P, Zavarise G. A mortar formulation for 3D large deformation contact using NURBS-based isogeometric analysis and the augmented Lagrangian method. *Computational Mechanics* 2012; **49**(1):1–20.
36. Heegaard J, Curnier A. An augmented Lagrangian method for discrete large slip contact problems. *International Journal for Numerical Methods in Engineering* 1993; **36**:569–593.
37. O'Rourke J. *Computational Geometry in C*, 2nd ed. Cambridge University Press: Cambridge, 1998.
38. Hintermüller M, Ito K, Kunisch K. The primal–dual active set strategy as a semismooth Newton method. *SIAM Journal on Optimization* 2003; **13**:865–888.
39. Stupkiewicz S, Lengiewicz J, Korelc J. Sensitivity analysis for frictional contact problems in the augmented Lagrangian formulation. *Computer Methods in Applied Mechanics and Engineering* 2010; **199**:2165–2176.
40. OOfelie. Object oriented finite elements led by interactive executor. Open Engineering. S.A., 2010. (Available from: http://www.open-engineering.com).
41. SAMCEF. Mecano V13 user manual. Samtech S.A., 2007. (Available from: http://www.samtech.com).
42. Chen X, Hisada T. Development of a finite element contact analysis algorithm to pass the patch test. *Japan Society of Mechanical Engineers* 2006; **49**:483–491.
43. Johnson K. *Contact Mechanics*. Cambridge University Press: Cambridge, 1987.
44. Cavalieri F. Multiaxial fatigue and wear design in mechanical componentes at high temperature. *Thesis*, Universidad Nacional del Litoral, 2010. (Available from: http://bibliotecavirtual.unl.edu.ar:8180/tesis/handle/1/200).

DOI: 10.1002/nme